City Research Online

City, University of London Institutional Repository

Article

Numerical CFD Simulations and Indicated Pressure Measurements on a Sliding Vane Expander for Heat to Power Conversion Applications

Giuseppe Bianchi [1,]*[ ], **Sham Rane** [2], **Fabio Fatigati** [3], **Roberto Cipollone** [3][ ] **and Ahmed Kovacevic** [4]

[1] RCUK Centre for Sustainable Energy use in Food chains (CSEF), Institute of Energy Futures, Brunel University London, Uxbridge UB8 3PH, UK

[2] Department of Engineering Science, University of Oxford, Oxford OX2 0ES, UK

[3] Department of Industrial and Information Engineering and Economics, University of L'Aquila, 67100 L'Aquila, Italy

[4] School of Mathematics, Computer Science and Engineering, City, University of London, London EC1V 0HB, UK

[*] Correspondence: giuseppe.bianchi@brunel.ac.uk; Tel.: +44-1895-267-707

check for updates

Abstract: The paper presents an extensive investigation of a small-scale sliding vane rotary expander operating with R245fa. The key novelty is in an innovative operating layout, which considers a secondary inlet downstream of the conventional inlet port. The additional intake supercharges the expander by increasing the mass of the working fluid in the working chamber during the expansion process; this makes it possible to harvest a greater power output within the same machine. The concept of supercharging is assessed in this paper through numerical computational fluid dynamics (CFD) simulations which are validated against experimental data, including the mass flow rate and indicated pressure measurements. When operating at 1516 rpm and between pressures of 5.4 bar at the inlet and 3.2 bar at the outlet, the supercharged expander provided a power output of 325 W. The specific power output was equal to 3.25 kW/(kg/s) with a mechanical efficiency of 63.1%. The comparison between internal pressure traces obtained by simulation and experimentally is very good. However, the numerical model is not able to account fully for the overfilling of the machine. A comparison between a standard and a supercharged configuration obtained by CFD simulation shows that the specific indicated power increases from 3.41 kW/(kg/s) to 8.30 kW/(kg/s). This large power difference is the result of preventing overexpansion by supercharging. Hence, despite the greater pumping power required for the increased flow through the secondary inlet, a supercharged expander would be the preferred option for applications where the weight of the components is the key issue, for example, in transport applications.

Keywords: sliding vane expander; positive displacement expander; waste heat recovery; dynamic computational grid; user defined nodal displacement; CFD; indicated pressure; ORC; R245fa

1. Introduction

The expander is a crucial component of Organic Rankine Cycle (ORC) systems due to its impact on cycle efficiency. The key parameters to consider during the selection of an expander are: isentropic efficiency, lubrication requirements, reliability, and cost [1]. On a medium–large scale, ORC power plants employ turbomachines. On the other hand, in small-scale ORC applications, positive displacement expanders are generally preferred due to their capability to operate with small mass flow rates and

high pressure ratios. A thorough review on the recent advances in positive displacement expander technologies can be found in [2].

Rotary vane expanders are one of the available positive displacement expander technologies, characterized by a flat efficiency curve. This feature makes vane machines suitable to deal with two-phase workings fluids [3,4]. Moreover, they require little maintenance and lubrication [1] and they can be hermetically sealed [5]. Their simple geometrical structure and small number of moving parts further impact the competitive advantage of this technology in terms of lower capital and operational costs. Previous experimental activities on vane expanders reported efficiencies between 40% and 58% when operating with hexamethyldisiloxane [6]; the maximum efficiency achieved by a micro-ORC expander using R123 instead reached 70% [7].

Compared to other positive displacement technologies, vane expanders experience significant friction and volumetric losses [8]. The main sources of friction losses are the ones between the stator and the tips of the blades that are pulled out from the rotor slots due to centrifugal force. On the other hand, the main source of volumetric losses is the gap between the stator (fixed cylinder) and rotor (rotating cylinder), since the geometrical tangency between these components cannot be fulfilled in practice due to manufacturing tolerances [9]. Another issue identified in [10] was the blade instability during its rotation. In fact, should the hydrodynamic contact with the stator surface be not constantly ensured because of vibrations or fluid pressure forces, the cells separated by the blade would be connected. Hence, substantial leakage from high- to low-pressure cells would take place. These phenomena would eventually lead to an alteration of the built-in volume ratio, since when adjacent cells are connected the closed volume expansion phase is shortened [11]. A further limiting aspect of this machine is the fixed built-in volume ratio, due to the geometrical feature of the machine where the suction and discharge ports are machined on the stator. This limitation was overcome in [12] through an actuator that varied the outlet opening angle of the discharge port.

The concept of supercharging a vane expander was proposed in [13–15], with the aim of increasing the power output of a given machine. Supercharging the expander requires an additional suction port along the closed-volume expansion phase to supply a larger quantity of working fluid at the same suction conditions as the main inlet. The enthalpy carried out by this additional mass leads to an increase of the cell pressure and, in turn, to a greater indicated power. In [13], an optimization study carried out using a one-dimensional modeling methodology made it possible to identify the angular location and the extent of the supercharging port that maximized the expander mechanical power output up to 50% more than a standard machine. In [14], an experimental comparison between single and dual intake expanders was carried out at a constant manometric expansion ratio. The results showed an increase of power output of 50% using an additional 40% of mass flow rate. In [15], an analytical formulation was developed to demonstrate that supercharging the expander also improves its efficiency.

In order to achieve a deeper understanding of the supercharging process and its impact on the machine operation, the current research activity aimed at performing numerical 3D computational fluid dynamics (CFD) simulations on the machine was developed and tested in [13–15]. An essential requirement to carry out numerical CFD simulations in a vane machines is the development of algorithms to discretize the computational fluid domain of the expander cells. The deforming grid generation methodology was developed in [16,17] and further improved in [18] by using differential techniques instead of algebraic ones. The advantages of a differential approach are better cell quality in terms of orthogonality, smoothness, and area ratio. The grid generation has been implemented in the customized grid generation tool SCORG [19,20]. The results show not only the successful model validation but also an extensive comparison between standard and supercharged machines.

2. Experimental Activity

2.1. Test Rig and Measurement Chain

The supercharged expander was tested in an automotive ORC loop at the University of L'Aquila, operating with R245fa. The plant layout is reported in Figure 1 and shown in Figure 2. Besides the vane expander, the ORC system had no recuperation and relied on a plate heat exchanger as a condenser and a gear pump. Downstream of the finned tube heat recovery vapor generator (HRVG) the flow was split to feed both the suction lines. In particular, the supercharging line could be closed using a ball valve. The expander was directly coupled with an asynchronous electric generator, which constrained the expander to rotate at revolution speeds slightly higher than 1500 rpm when the machine was connected to the electric grid. Further details on the test rig can be found in [14,15].
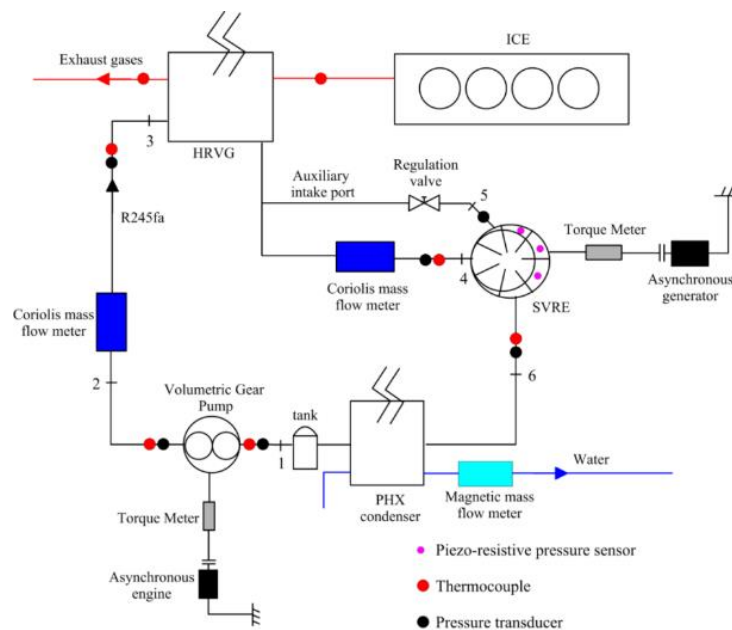

Figure 1. Experimental layout.

Figure 2. ORC (Organic Rankine Cycle) test rig.

From an instrumentation perspective, two Coriolis mass flow meters were installed downstream of the pump and on the primary inlet of the expander. Pressure and temperature transducers were located across each component of the ORC loop. The expander performance was eventually measured

through a torque meter and a set of three piezo-resistive pressure transducers, whose positions are reported in Figure 3. The overall expander dimensions and port positioning are summarized in Table 1. As can be observed from Figure 1, the dual intake phase started immediately after the end of the main one. Indeed, the difference between the dual intake port opening angle and the main intake port closing angle is equal to the angular vane extent. This position, as it was demonstrated in [13,15], made it possible to maximize the mechanical power produced.
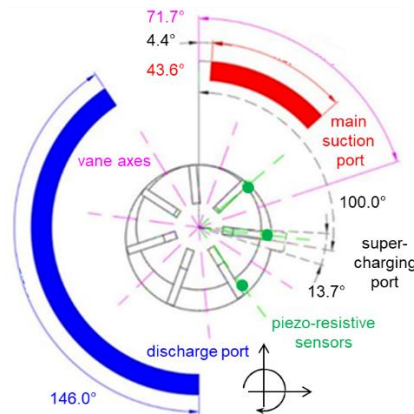

Figure 3. Ports and sensors positioning [5].

Table 1. Expander geometry.

Number of Chambers	7
Stator Inner Diameter	76.00 mm
Rotor Outer Diameter	65.00 mm
Eccentricity	5.45 mm
Chamber Width	60.00 mm
Blade length	17.00 mm
Blade thickness	3.96 mm
Intake port opening angle	4.4°
Intake port closing angle	48.0°
Exhaust port opening angle	180.0°
Exhaust port closing angle	320.0°

2.2. Test Campaign

Three test cases were selected for the CFD validation. A summary is reported in Table 2. Depending on the opening of the ball valve upstream of the secondary inlet, different supercharging ratios could be achieved. The distribution of the mass flow rates directly affected the inlet pressures.

Table 2. Experimental campaign with measurement uncertainty.

	Test Case #1			Test Case #2			Test Case #3		
	p	T	m	p	T	m	p	T	m
	±0.3 bar$_a$	±0.3 °C	kg/s	±0.3 bar$_a$	±0.3 °C	kg/s	±0.3 bar$_a$	±0.3 °C	kg/s
Main inlet (m ± 0.15%)	4.55	66.1	0.047	5.44	94.3	0.061	5.57	82.3	0.055
Superch. Inlet (m ± 0.05%)	4.75	66.1	0.054	4.74	94.3	0.039	5.77	82.3	0.064
Outlet	3.10	58.6		3.21	85.9		3.60	73.5	
Rev. speed (±1 rpm)	1511			1516			1517		
Torque (±0.02 Nm)	1.50			2.05			2.11		

p, absolute pressure; T, temperature; m, mass flow rate.

The operating point that was selected to show the validation of the CFD results was test case #2, even though the validation was successful for all the operating points. In this point, there was limited supercharging, which in turn led to a 1 bar pressure difference between the suction conditions of the primary line and the ones related to the supercharging port.

3. CFD Modeling

A CFD modeling approach of user defined nodal displacement [18] was applied for the moving and deforming fluid domain enclosed between the rotor, stator, and blades of a vane machine. Nodal locations for each time step were calculated externally, prior to the numerical flow solution in the CFD solver using SCORG. Figure 4 represents the workflow of the grid generation algorithm. Further details are also presented in Figure 5.
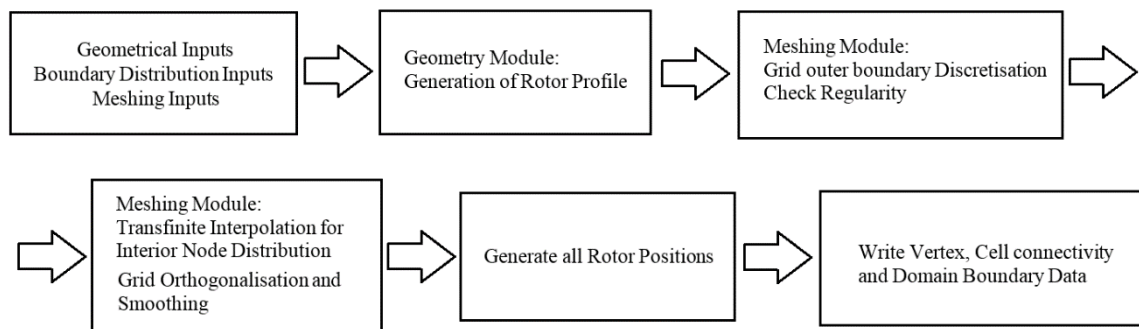

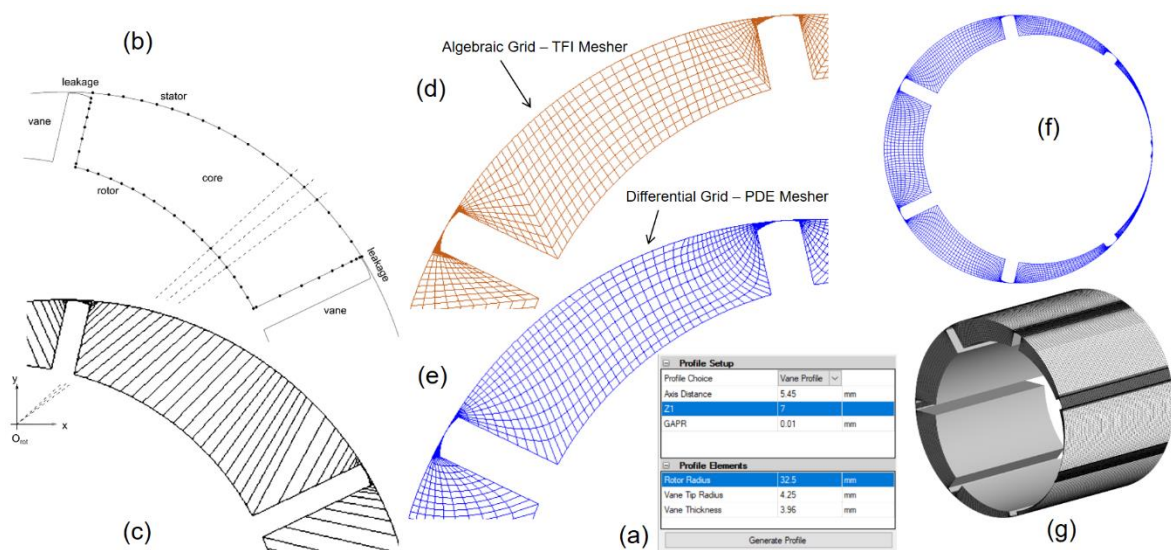**Figure 4.** Main blocks of the vane rotor grid generation program.

Figure 5. Grid generation steps: (**a**) parametric profile generation, (**b**) boundary discretization, (**c**) stretching function application, (**d**) algebraic grid generation, (**e**,**f**) differential grid generation, (**g**) 3D vane rotor grid.

In [16], a parametric geometry program built as a Matlab application was used to produce the rotor profile, along with the vane at the initial rotor position. A parametric profile generation was implemented in SCORG in the current study and the required input parameters are shown in Figure 5a. For a given set of rotor and stator diameters, number of vanes, and vane thickness, the program provided coordinates of the points of the chamber boundaries. This profile was an input to the meshing algorithm. Successive rotor positions appeared to be rigid body rotations for the rotor, while for the fluid volume that was deforming, it was a complex boundary motion where the rotor rotated, the stator was stationary, and each of the vanes underwent a general body motion. For simplification, variable

blade tip clearance gap changes were not accounted for the presented analysis, but the meshing algorithm created the possibility to further introduce an angular gap variation.

With reference to Figure 5b, the grid generation procedure worked on the 2D cross sections of the rotating and deforming fluid domain and then replicated along the axial direction to get the 3D mesh (Figure 5g). In particular, the reference fluid domain was the one enclosed between the stator, rotor, and blades (Figure 5b). The developed grid generation methodology aimed at producing a computational grid that fulfilled the topology of an 'O' grid, since this structure avoids any inaccuracies that can be introduced due to a non-matching mesh connection between the core and leakage regions of the so-called rotor mesh. Prior to the distribution of the computational nodes, the grid boundary was reconstructed through analytical relationships that described the trajectories of the rotor, stator, and blades points. This approach provided flexible and parametric features to the overall procedure since it made it easy to model any vane machine geometry. The geometrical data of the expander that was used to generate the rotor boundary are listed in Table 3. The discretization of the rotor grid boundaries is shown in Figure 5b and considers different numbers of nodes for vane tip, vane sides, and rotor locations. The specified nodes were then distributed on the various parts of the segments using control functions. The total number of nodes used for discretization of the rotor boundary was maintained for the discretization of the stator boundary. The sudden transition from the leakage gaps to the core was handled by the introduction of stretching functions that gradually flared the radial mesh lines from leakage gap into the core, as seen in Figure 5c.

Table 3. Summary of geometrical and mesh properties of the expander model.

Geometry		Mesh	Ports	Rotor
Rotor Diameter	65 mm	Cell type	Tetrahedral	Hexahedral
Stator Diameter	76 mm	Node count (Million)	0.143	0.157
Axial Length	60 mm	Maximum aspect ratio	23	228
Tip Clearance	10 μm	Minimum orthogonality	10.0	11.6

Figure 5d shows the quadrilateral cells in a 2D cross-section generated by an initial algebraic technique using a trans-finite interpolation (TFI) mesher, where the continuous mesh between the tip leakage gaps and the core cells formed between the vanes meant that the number of cells covering the radial direction from the rotor boundary to the stator one remained unchanged [17]. Figure 5e shows the improved cell quality with smooth cells generated using a differential technique with a partial differential equation (PDE) mesher of the Poisson's form [19]. A hexahedral 3D grid is shown in Figure 5g.

Figure 6 presents the CFD model of the vane expander, along with the addition of the supercharged inlet, which is of significant interest in the current study. Tetrahedral mesh was used for the static ports of the expander, as seen in the cross-section of the mesh represented in Figure 7. The high-pressure main inlet, supercharged inlet, low-pressure outlet, and the axial interface of the low-pressure port with the deforming rotor domain have been highlighted by the color scheme. All these interfaces were set in the ANSYS CFX solver as non-conformal conservative flux types of fluid–fluid interfaces. Table 3 also summarizes the properties of rotor and ports grids while Table 4 presents the details of the CFD solver's numerical setup. The operating conditions that were considered as the benchmark for this case were 1551 rpm as the revolution speed and 5.44 bar$_a$ as inlet pressure, with 94.3 °C as the inlet gas temperature. The supercharged inlet pressure was 4.74 bar$_a$ with 94.3 °C gas temperature. The outlet pressure was 3.21 bar$_a$. The Aungier Redlich Kwong real gas model was used to specify the coefficients of the polynomials to define the material properties and equation of state. Coefficients for specific heat (R245fa) and critical state temperature and pressure were supplied to generate a lookup table in the temperature range of 273 and 400 K, while the pressure range was between 2.0 and 60.0 bar$_a$.
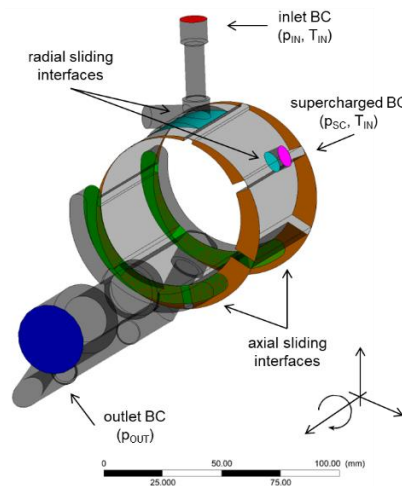
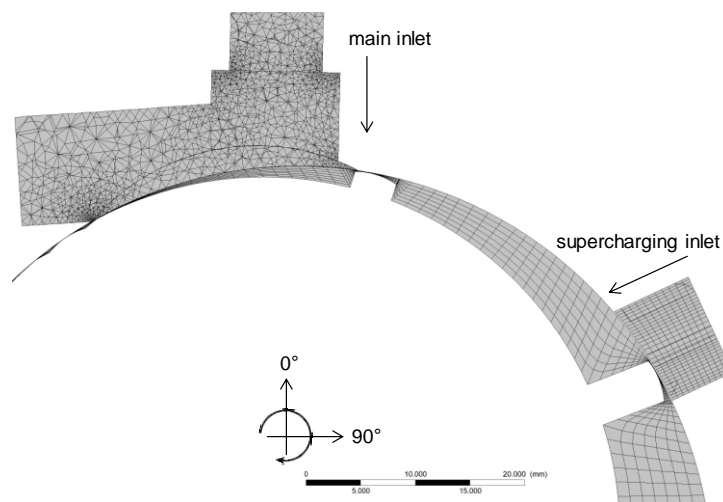**Figure 6.** CFD model of the vane expander with supercharged inlet.

Figure 7. Detail in a cross-section of the static and deforming grids.

Table 4. Details on the numerical setups in the ANSYS CFX solver.

Mesh Deformation	User Defined Nodal Displacement	Advection Scheme	High Resolution
Mesh in ports	Tetrahedral with boundary layer refinements (ANSYS Mesh)	Transient scheme	Second order Backward Euler
Turbulence model	SST – k Omega (Standard Wall Functions)	Transient inner loop coefficients	Up to 20 iterations per time step
Inlet/Supercharge boundary condition	Opening (Specified total pressure and temperature)	Convergence criteria	r.m.s residual level 1e^{-03}
Outlet boundary condition	Opening (Static pressure. In the case of backflow used as total pressure and temperature)	Relaxation parameters	Solver relaxation fluids (0.4)

ANSYS CFX provides a coupling feature called a junction box routine that is a user defined library to specify mesh deformation from custom applications such as SCORG. The solver updates the node coordinates from a set of pre-generated coordinate files after every crank angle step (or its submultiples). Solver time step size finally results from the selected crank angle step (at which the customized grids are generated) and revolution speed of the rotor. In this case study, the full rotation of the rotor was defined by 720 grid positions. This resulted in an angular step of 0.5° per solver step. Hence, to achieve a rotational speed of 1551 rpm, the time step size was set to $5.3728 \times e^{-5}$ s. In these conditions, the RMS Courant number of the coupled solver during the calculations was in a

range between 7.0 and 8.0, while the maximum Courant number was in the order of 110.0 at all time steps. Therefore, the Courant–Friedrichs–Lewy (CFL) condition for the convergence of the numerical resolution of the partial differential equations was ensured.

4. Results and Discussion

Each of the three experimental points listed in Table 2 were simulated in an eight-core workstation with an i7-6700 CPU at 3.40 GHz. RAM usage was 2.8 GB. The parallel simulation run in dual precision required nearly 22 h to complete two full revolutions of the expander (1440 time steps), initialized with previous results to speed up the computation. A series of monitoring points were required to retrieve the indicated pressure. The comparison of the experimental and simulation data is presented in Figure 8, Figure 9, and Figure 10a. Unlike in the activities presented in [21], where piezo-electric pressure transduces were used, the use of piezo-resistive transducers made it possible to reconstruct the final experimental curve, reported in black in Figures 8 and 9, without applying any pressure offset to measured data. In particular, the final experimental trace results from the combination of pressure traces related to the three angular ranges, in which the pressure in the same rotating cell was consecutively measured by the three pressure transducers, are shown in Figures 1 and 3.
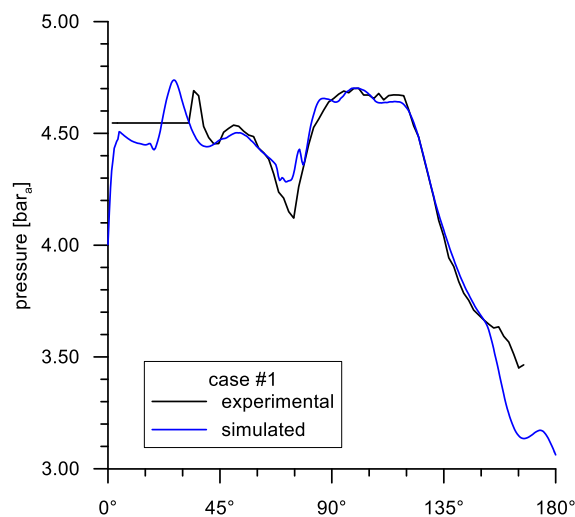

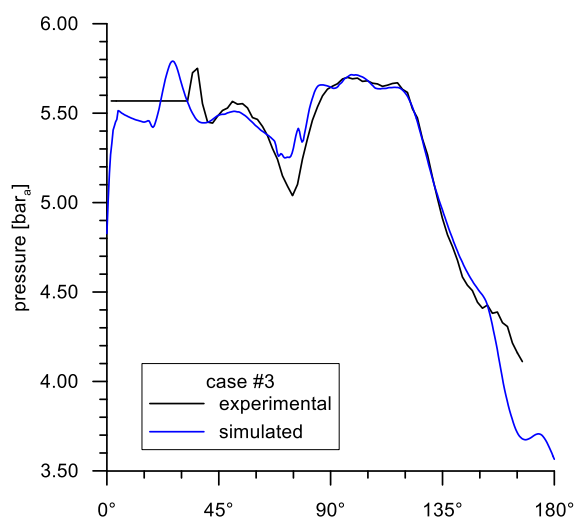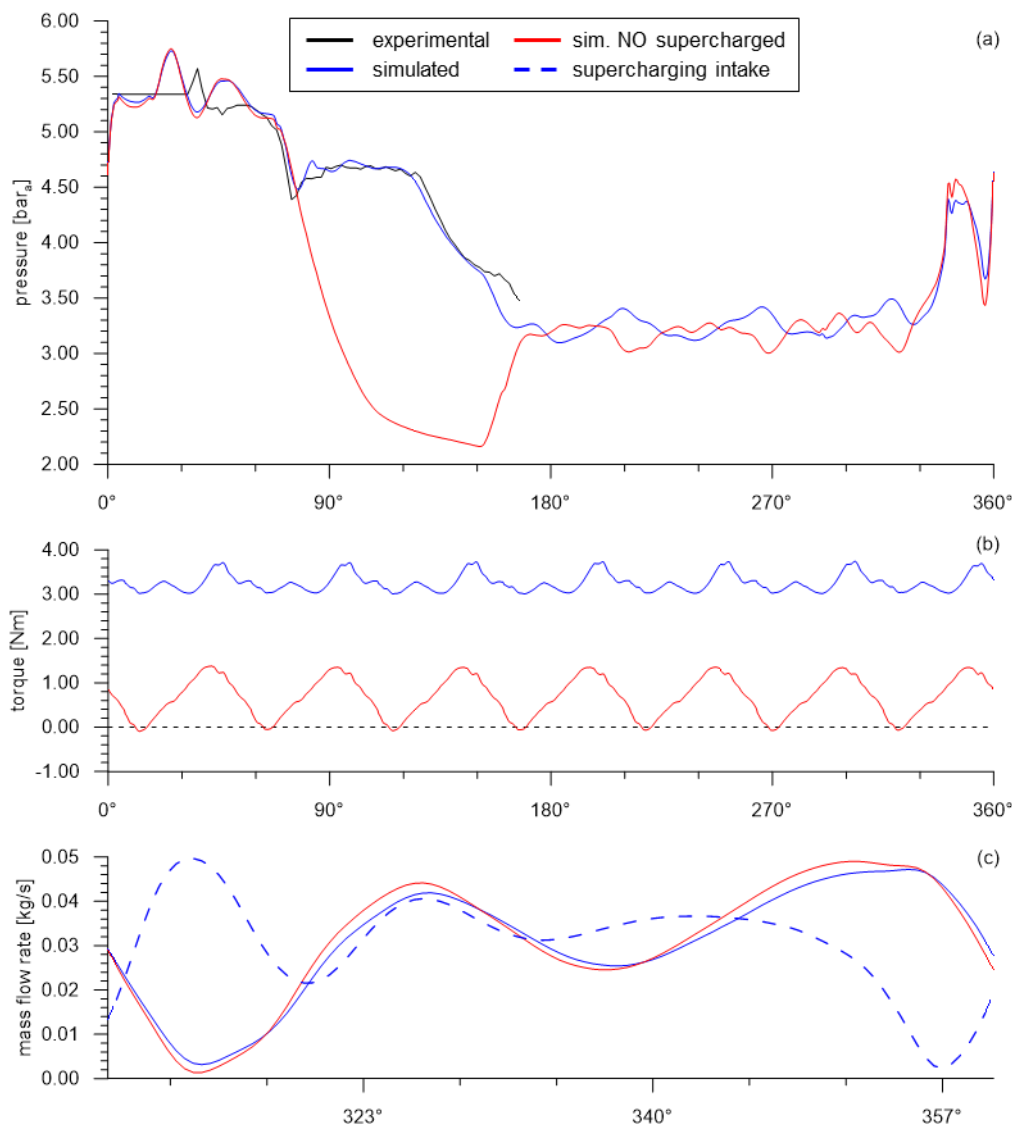**Figure 8.** Angular pressure traces in case #1.

Figure 9. Angular pressure traces in case #3.

Figure 10. Analysis of test case #2: comparison between experimental and numerical results, with and without supercharging in terms of angular pressure evolution (**a**), torque (**b**), and mass flow rates (**c**) at the main (continuous line) and supercharging (dashed line) ports.

The comparison of the internal pressure diagrams is good, given the simplification introduced in the modeling methodology (e.g., no leakage paths at the end wall plates or between adjacent blades). The charts clearly show the effect of the supercharging on the cell pressure. For instance, with reference to case #2 of Figure 10a, after the main suction process, the fluid expanded for a certain angle of the vane rotation from 5.3 bar to 4.4 bar. After the second intake process started, while the internal volume was still increasing, the pressure increased. Depending on the suction pressures, the supercharging effect can be higher or lower, as shown for cases #1 and #3 in Figures 8 and 9, respectively. In any case, the increase in the internal pressure led to some under expansion due to the mismatch between the discharge pressure (i.e., condenser pressure of the ORC system) and the pressure at the end of the internal expansion process. However, this delivers significantly higher power. The experimental values before 45° show a constant pressure trend that was not measured by the piezo-resistive transducers, but a low frequency pressure transducer at the inlet duct. These values were used to set up the inlet pressure boundary conditions of the simulations.

Besides the comparison between the experimental and numerical results, Figure 10 shows a benchmark of the supercharged case, with a standard expander configuration that was simulated

using the same boundary conditions. The pressure traces in Figure 10a show that the indicated pressure was affected by the supercharging only during the closed volume expansion phase. In fact, a good overlapping between the blue (supercharged) and red (standard) curves can be noticed. This implies that even the main intake process is not affected by the supercharging, as shown in Figure 10c, which reports the area averaged instantaneous mass flow rate at the suction ports and with reference to the last vane passage, i.e., from 308.5° to 360°. The comparison between the continuous and dashed blue lines further shows the correct positioning of the supercharging port, since the peak maximum mass flow rates were shifted of a quantity equal to at least a vane passage (51.42°). In addition, it can be noticed that in the standard configuration, due to the over-expansion, the delivered power was low, while for the supercharged expander, the power was significantly increased.

Without supercharging, with the boundary conditions of case #2, there would have been an over-expansion of the fluid trapped in the cells with a magnitude of 1.1 bar. The recompression of the working fluid from 135° to 180° would have required a significant power input that, in turn, would have been discounted from the net power output available at the expander shaft. Therefore, the area between the red and blue curves gives an indication of the additional indicated power achievable through the supercharging. Evidence of these benefits can be also noticed in the torque trends referred to in the last cycle simulated. In the case of supercharging, the torque curve not only becomes higher but also smoother. The reduction of the amplitude in the torque curve from 1.1 Nm to 0.5 Nm would also provide significant structural benefits with regards to vibrations and component lifetime.

Table 5 presents a summary of the experimental and numerical performance in the selected test cases. There is a substantial discrepancy between the measured and simulated mass flow rates, even though the indicated pressure match is acceptable. In particular, the experimental values are always greater than the ones resulting from the simulations. This difference is likely due to the fact that the expander was overfilled compared to its volumetric capacity. The additional mass flow rate did not produce any mechanical work but was simply laminated through the clearance gaps that, however, have not been modeled (e.g., end wall plates, rotor slots).

**Table 5.** Summary of the experimental and numerical results.

	Case #1		Case #2			Case #3	
	exp.	sim.	exp.	sim.	sim. NO SC	exp.	sim.
Inlet mfr (kg/s)	0.047	0.021	0.061	0.031	0.031	0.055	0.026
SC inlet mfr (kg/s)	0.054	0.045	0.039	0.031	N/A	0.064	0.052
Outlet T (°C)	58.6	58.8	85.9	81.0	74.0	73.5	71.0
Torque (Nm)	1.50	2.81	2.05	3.25	0.68	2.11	3.83
Spec. power (kW/(kg/s))	2.35	6.65	3.25	8.30	3.41	2.82	7.72
Mechanical efficiency	53.4%		63.1%		N/A	55.1%	

The lower outlet temperature values are instead justified by having assumed adiabatic walls.

The lower torque values instead are due to the measurement of the actual mechanical power in the experiments. On the other hand, the simulated values refer to the indicated torque, i.e., without any friction losses. As such, the ratio of the experimental and simulated torque provides a good estimation of the mechanical efficiency of the machine, which ranged between 53.4% and 63.1%. These values are quite encouraging with respect to other positive displacement expanders [1,2], especially if one considers that the prototype had hundreds of hours of operation.

The experimental specific power, calculated as the ratio of the mechanical power and sum of the two mass flow rates, ranged between 2.35 kW/(kg/s) and 3.25 kW/(kg/s). Instead, if one compares the simulations referred to case #2, the supercharging would lead to a specific power output increase from 3.41 kW/(kg/s) to 8.30 kW/(kg/s).

Figure 11 shows a comparison between supercharged and standard expanders, in terms of pressure and velocity fields and with reference to test case #2. For each design configuration, the figure reports a series of six snapshots, from 310° to 360°. At 310°, the pressure and velocity fields in the standard (Figure 11a) and supercharged (Figure 11g) configurations show significant differences due to the second intake. In the standard configuration, the cell has completed the suction process and starts the closed volume expansion phase reported in the frames (b–e). The flow field is aligned with the clockwise revolution sense, even though some recirculation areas can be noticed due to the leakage flows at the 10 μm gap between the blade tip and stator. In Figure 11g, the vortex shown in Figure 11a is instead replaced to the supercharged intake flow that moves against the revolution sense and fills the expander cell. In the remaining frames, an overall increase in pressure can be noticed due to the supercharging. Comparing the pressure fields at 350°, we can conclude that the lower differential pressure across the cells displayed implies, in the supercharged case, lower leakage flows. The frames related to the angular range 330–350° eventually show how the grid generation handles the computational region in the proximity of the sealing arc in order to get an O-grid.
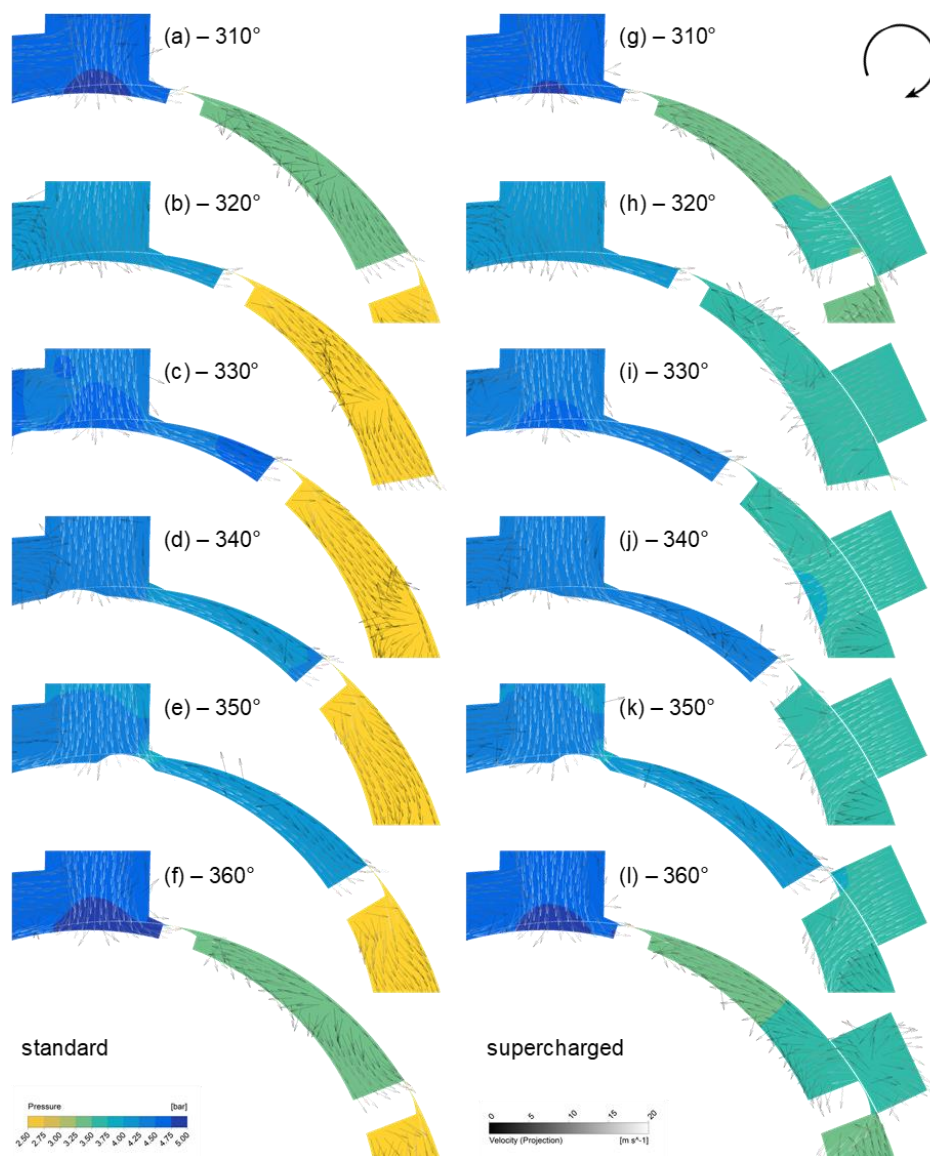
Figure 11. Comparison of standard and supercharged expanders CFD results in terms of pressure contours at mid-length with superimposed projected velocity field for the last vane passage simulated (310–360°). Simulation data refer to test case #2 in Table 2.

5. Conclusions

The research presented in this paper combined numerical and experimental methodologies to assess the potential of supercharging to enhance the power output in positive displacement expanders. This approach considered an additional intake to increase the mass flow rate and consequently to increase the internal pressure during the closed volume expansion process. In this paper, this approach was demonstrated for the rotary vane positive displacement expander.

The supercharged vane expander was tested in an ORC loop instrumented with piezo-resistive pressure transducers to retrieve the indicated pressure. Two Coriolis flow meters and a torque meter were used for measurement of the mechanical power output. Three test cases were selected from the large set of experimental results at various conditions in order to be compared with the numerical CFD simulations. The analytical grid generation method built in the software SCORG was used for numerical mapping of the rotating and deforming domain of the vane machine. These domains were connected to the primary and supercharging intake lines through sliding radial interfaces. The CFD solution was obtained with the commercial solver ANSYS CFX.

In all three test cases, the indicated pressure traces obtained by experiment and through simulation agreed well. However, a substantial difference in the mass flow rates was noticed due to the expander overfilling during the tests and the absence of axial leakage paths in the numerical model. The comparison of the pressure and velocity fields in the cases of a standard and a supercharged configuration showed significant differences. In particular, the lower differential pressure across the blade during the expansion process is expected to be beneficial for the reduction of the leakage flows. The amplitude of torque fluctuation at the expander shaft is additionally reduced in the case of supercharging, despite the under-expansion, which occurs as the working chamber opens towards the discharge port.

In the considered test case, supercharging the expander resulted in the increase of the specific power output from 3.41 kW/(kg/s) to 8.30 kW/(kg/s). The extremely large power difference is due to preventing overexpansion by supercharging.

References

1. Bao, J.; Zhao, L. A review of working fluid and expander selections for organic Rankine cycle. *Renew. Sustain. Energy Rev.* **2013**, *24*, 325–342. [CrossRef]
2. Imran, M.; Usman, M.; Park, B.S.; Lee, D.H. Volumetric expanders for low grade heat and waste heat recovery applications. *Renew. Sustain. Energy Rev.* **2016**, *57*, 1090–1109. [CrossRef]
3. Musthafah, M.T.; Yamada, N. Thermodynamic analysis of expansion profile for displacement-type expander in low-temperature Rankine cycle. *J. Therm. Sci. Technol.* **2010**, *5*, 61–74. [CrossRef]
4. Badr, O.; Probert, S.D.; O'Callaghan, P. Performances of multi-vane expanders. *Appl. Energy* **1985**, *20*, 207–234. [CrossRef]
5. Kolasiński, P.; Błasiak, P.; Rak, J. Experimental investigation on multi-vane expander operating conditions in domestic CHP ORC system. *Energy Procedia* **2017**, *129*, 323–330. [CrossRef]

6. Mascuch, J.; Novotny, V.; Vodicka, V.; Zeleny, Z. Towards development of 1–10 kW pilot ORC units operating with hexamethyldisiloxane and using rotary vane expander. *Energy Procedia* **2017**, *129*, 826–833. [CrossRef]

7. Kolasiński, P. The Influence of the Heat Source Temperature on the Multivane Expander Output Power in an Organic Rankine Cycle (ORC) System. *Energies* **2015**, *8*, 3351–3369. [CrossRef]

8. Fukuta, M.; Yanagisawa, T.; Radermacher, R. Performance prediction of vane type expander for CO_2 cycle. In Proceedings of the 21st International Congress of Refrigeration, Washington, DC, USA, 17–22 August 2003.

9. Yang, B.; Peng, X.; He, Z.; Guo, B.; Xing, Z. Experimental investigation on the internal working process of a CO2 rotary vane expander. *Appl. Therm. Eng.* **2009**, *29*, 2289–2296. [CrossRef]

10. Vodicka, V.; Novotny, V.; Mascuch, J.; Kolovratnik, M. Impact of major leakages on characteristics of a rotary vane expander for ORC. *Energy Procedia* **2017**, *129*, 387–394. [CrossRef]

11. Qiu, G.; Liu, H.; Riffat, S. Expanders for micro-CHP systems with organic Rankine cycle. *Appl. Therm. Eng.* **2011**, *16*, 3301–3307. [CrossRef]

12. Yan, J.; Han, Y.; Tian, J.; Xu, Y.; Zhang, Y.; Chen, R. Performance investigation of a novel expander coupling organic Rankine cycle: Variable expansion ratio rotary vane expander for variable working conditions. *Appl. Therm. Eng.* **2019**, *152*, 573–581. [CrossRef]

13. Fatigati, F.; Bianchi, G.; Cipollone, R. Development and numerical modelling of a supercharging technique for positive displacement expanders. *Appl. Therm. Eng.* **2018**, *140*, 208–216. [CrossRef]

14. Fatigati, F.; Di Bartolomeo, M.; Cipollone, R. Experimental and numerical characterization of a positive displacement vane expander with an auxiliary injection port for an ORC-based power unit. *Energy Procedia* **2018**, *148*, 830–837. [CrossRef]

15. Fatigati, F.; Di Bartolomeo, M.; Cipollone, R. Dual intake rotary vane expander technology: Experimental and theoretical assessment. *Energy Convers. Manag.* **2019**, *186*, 156–167. [CrossRef]

16. Bianchi, G.; Rane, S.; Kovacevic, A.; Cipollone, R. Deforming grid generation for numerical simulations of fluid dynamics in sliding vane rotary machines. *Adv. Eng. Softw.* **2017**, *112*, 180–191. [CrossRef]

17. Bianchi, G.; Rane, S.; Kovacevic, A.; Cipollone, R.; Murgia, S.; Contaldi, G. Numerical CFD simulations on a small-scale ORC expander using a customized grid generation methodology. *Energy Procedia* **2017**, *129*, 843–850. [CrossRef]

18. Rane, S.; Kovacevic, A. Application of numerical grid generation for improved CFD analysis of multiphase screw machines. In Proceedings of the IOP Conference Series: Materials Science and Engineering, Beijing, China, 24–27 October 2017.

19. Kovacevic, A.; Stosic, N.; Smith, I. *Screw Compressors—Three Dimensional Computational Fluid Dynamics and Solid Fluid Interaction*; Springer Science and Business Media: New York, NY, USA, 2006; ISBN 978-3-540-36302-6.

20. Kovacevic, A. Boundary adaptation in grid generation for CFD analysis of screw compressors. *Int. J. Numer. Methods Eng.* **2005**, *64*, 401–426. [CrossRef]

21. Bianchi, G.; Cipollone, R. Friction power modeling and measurements in sliding vane rotary compressors. *Appl. Therm. Eng.* **2015**, *84*, 276–285. [CrossRef]